scientific reports

OPEN

Soret–Dufour impact on a three-dimensional Casson nanofluid flow with dust particles and variable characteristics in a permeable media

Naila Shaheen[1], Muhammad Ramzan[1], Ahmed Alshehri[2], Zahir Shah[3,4✉] & Poom Kumam[5,6✉]

In this study, the effects of variable characteristics are analyzed on a three-dimensional (3D) dusty Casson nanofluid flow past a deformable bidirectional surface amalgamated with chemical reaction and Arrhenius activation energy. The surface is deformable in the direction of the *x*-axis and *y*-axis. The motion of the flow is induced due to the deformation of the surface. The impression of Soret and Dufour's effects boost the transmission of heat and mass. The flow is analyzed numerically with the combined impacts of thermal radiation, momentum slip, and convective heat condition. A numerical solution for the system of the differential equations is attained by employing the bvp4c function in MATLAB. The dimensionless parameters are graphically illustrated and discussed for the involved profiles. It is perceived that on escalating the Casson fluid and porosity parameters, the velocity field declines for fluid-particle suspension. Also, for augmented activation energy and Soret number, the concentration field enhances. An opposite behavior is noticed in the thermal field for fluctuation in fluid-particle interaction parameters for fluid and dust phase. Drag force coefficient increases on escalating porosity parameter and Hartmann number. On amplifying the radiation parameter heat and mass flux augments. A comparative analysis of the present investigation with an already published work is also added to substantiate the envisioned problem.

Nomenclature

b	Positive constant
B_0	Magnetic field strength
c	Positive constant
c_s	Concentration susceptibility
c_p	Specific heat capacity of the fluid
C_w	Concentration at the surface
C_∞	Fluid ambient concentration
c_m	Specific heat of dust particle
C_f	Skin friction coefficient
D_T	Thermophoretic diffusion coefficient
D_B	Brownian diffusion coefficient

[1]Department of Computer Science, Bahria University, Islamabad 44000, Pakistan. [2]Department of Mathematics, Faculty of Sciences, King Abdulaziz University, Jeddah 21589, Saudi Arabia. [3]Department of Mathematical Sciences, University of Lakki Marwat, Lakki Marwat, Khyber Pakhtunkhwa 28420, Pakistan. [4]Center of Excellence in Theoretical and Computational Science (TaCS-CoE), Faculty of Science, King Mongkut's University of Technology Thonburi (KMUTT), 126 Pracha Uthit Rd., Bang Mod, Thung Khru, Bangkok 10140, Thailand. [5]Fixed Point Research Laboratory, Fixed Point Theory and Applications Research Group, Center of Excellence in Theoretical and Computational Science (TaCS-CoE), Faculty of Science, King Mongkut's University of Technology Thonburi (KMUTT), 126 Pracha Uthit Rd., Bang Mod, Thung Khru, Bangkok 10140, Thailand. [6]Department of Medical Research, China Medical University Hospital, China Medical University, Taichung 40402, Taiwan. ✉email: zahir@ulm.edu.pk; poom.kum@kmutt.ac.th

$D_B(C)$	Variable molecular diffusivity
$D_{B\infty}$	Ambient diffusion coefficient
d	Variable thermal conductivity parameter
$D_f = \frac{D_T k_t^*(C_w - C_\infty)}{\nu c_s c_p (T_w - T_\infty)}$	Dufour number
E_a	Activation energy
$E = \frac{E_a}{kT}$	Activation energy parameter
e	Variable molecular diffusivity parameter
h_1	Convective heat transfer coefficient
$Ha = \frac{\sigma B_o^2}{\rho c}$	Hartmann number
$H_1 = \frac{h_1}{k_\infty}\sqrt{\frac{\nu}{c}}$	Heat transfer Biot number
$K = 6\pi\mu r$	Stoke's drag constant
$k(T)$	Temperature-dependent thermal conductivity
$\bar{k}$	Mean absorption coefficient
K^*	Permeability of porous medium
k_r^2	Chemical reaction parameter
k_t^*	Thermal diffusion
$L = S\sqrt{\frac{c}{\nu}}$	Velocity slip parameter
m	Mass of dust particle
n	Fitted rate constant
$N_b = \frac{\tau(C_w - C_\infty)D_B}{\nu}$	Brownian motion parameter
$N_t = \frac{\tau D_T(T_w - T_\infty)}{\nu T_\infty}$	Thermophoretic parameter
Nu_x	Local Nusselt number
$P = \frac{b}{c}$	Stretching ratio parameter
$\Pr = \frac{\mu c_p}{k_\infty}$	Prandtl number
q_r	Radiative heat flux
Q_w	Heat flux
Q_m	Mass flux
$Re = \frac{c(x+y)^2}{\nu}$	Local Reynold number
$Rd = \frac{4\bar{\sigma}T_\infty^3}{\bar{k}k_\infty}$	Radiation parameter
r	The radius of a dust particle
S	Velocity slip factor
$S_c = \frac{\nu}{D_B}$	Schmidt number
$S_r = \frac{D_T k_t^*(T_w - T_\infty)}{\nu T_m(C_w - C_\infty)}$	Soret number
Sh_x	Local Sherwood number
T	Temperature of fluid
T_p	The temperature of the dust particle
T_w	The temperature at the surface of a sheet
T_∞	Fluid ambient temperature
u, v, w	Component of velocity
u_p, v_p, w_p	The velocity of dust particles
x, y, z	Cartesian coordinate

Greek symbols

ρ	Fluid density
$\lambda = \frac{Nm}{\rho}$	Mass concentration of dusty granules
σ_1	Electrical conductivity
β	Casson parameter
τ	The quotient of effective heat capacity of nanoparticle to the heat capacity of liquid
$\tau_v = \frac{m}{K}$	The relaxation time of the dust particle
$\rho_p = mN$	The density of dust particle
$\bar{\sigma}$	Stefan Boltzmann constant
$\lambda_1 = \frac{\nu}{K^* c}$	Porosity parameter
$\delta_v = \frac{1}{\tau_v c}$	Fluid particle interaction parameter for velocity
τ_T	Thermal equilibrium time
ν	Kinematic viscosity
ζ	Dimensionless variable
$\alpha = \frac{T_w - T_\infty}{T_\infty}$	Temperature difference
$\gamma = \frac{c_p}{c_m}$	The ratio of specific heat
$\delta = \frac{k_r^2}{c}$	Dimensionless reaction rate
τ_{zx}	Shear stress in the x-direction
τ_{zy}	Shear stress in the y-direction

The dusty fluid is formed with the amalgamation of dust granules with base fluid. Researchers have immensely emphasized fluid-particle suspension past an elongated surface as it has enormous applications in industry, engineering, and in the field of medicine such as power technology, cooling of nuclear reactors, power plant piping, retrieval of crude oil, sedimentation process, wastewater treatment, the formation of raindrops, emission of smoke from vehicles and environmental pollution. Hady and Mahdy[1] presented the convective flow of an electrically conducting dusty Micropolar fluid in a porous chamber with convective heat conditions. It is observed here that the temperature field of dusty granules elevates on incrementing the fluid-particle interaction parameter. A numerical solution for time-independent two-phase Jeffery fluid flow is presented by Zokri et al.[2] past a shrinking surface. The flow is incorporated with the effect of suction and Newtonian heating. It is found that the velocity of dusty flow upsurges on increasing the fluid-particle interaction parameter, whereas, for fluid flow, an opposite behavior is observed. Bio convective dusty nano liquid flow is numerically probed by Dey et al.[3] over a vertical elongated surface. It is reported that the concentration of microorganisms augments for rising values of the Brownian motion parameter. Bibi et al.[4] numerically inspected time-dependent nonlinear radiative two-phase pseudoplastic fluid flow over an elongated surface. It is perceived that enhancing the nonlinear thermal radiation parameter temperature for both phases escalates. Subsequently, exploration in this regard with different physical aspects can be seen in Refs.[5–9].

In the fluid flow, two mechanisms are involved in the conduction of heat. First, when the collision amid the molecules increases. Second, thermal conductivity plays a key role in escalating the random movement among the molecules. Thermal conductivity has significant applications in steam generators, electrolytes, concrete heating, and laminating. The characteristics of temperature-dependent thermal conductivity assimilated with mass diffusion on a radiative Casson fluid embedded in a porous medium past an elongated surface are analytically exhibited by Sohail et al.[10]. The findings disclosed that on escalating the Hartmann number and thermal radiation parameter, thermal field upsurges. The time-dependent flow of Pseudoplastic fluid past an extendable surface incorporated with homogeneous heterogeneous (h–h) reaction is numerically scrutinized by Hamid[11]. In this study, a substantial upsurge is noticed in the temperature field on augmenting the variable thermal conductivity. The features of the heat flux model on a time-independent 3D flow of non-Newtonian fluid are studied by Ramadevi et al.[12] with irregular heat source/sink past an elongated surface. It is noticed that the coefficient of mass transfer upsurges for rising values of the chemical reaction and stretching ratio parameter. Lu et al.[13] analytically explored the outcome of temperature-dependent thermal conductivity combined with nonlinear thermal radiation on a magnetohydrodynamic Oldroyd-B nanofluid flow over a bidirectional elongated sheet with robin conditions. Further analysis of temperature-dependent thermal conductivity is mentioned in Refs.[10,14–22].

The Soret–Dufour factor plays a key role in the transmission of heat and mass on a moving fluid. It has a vital role in several applications which include the design of nuclear reactors, geothermal energy, groundwater pollutant migration, oil reservoirs, isotopes separation, manufacture of rubber and plastic sheets, the mixture of gases, compact heat insulation exchanger, and nuclear waste disposal. Radiative flux with Soret–Dufour effect on a Darcy Forchheimer (DF) nano liquid flow past a linear elongated sheet is illustrated by Rasool et al.[23]. It is noticed that for growing values of Soret number, solutal field augments. Similar behavior is observed in the thermal field for the Dufour number. Using the Boungirono model Prasad et al.[24] explored the mechanism of Soret–Dufour effect on a 3D convective Oldroyd-B fluid flow past a deforming surface with velocity slip and convective heat condition. It is reported that fluid velocity upsurges on incrementing the Deborah number. On a Micropolar nanofluid flow, Ibrahim et al.[25] investigated the impact of the Soret and Dufour factor with multiple slip conditions past a bidirectional surface. The characteristic of heat and mass transfer on a mixed convective Jeffery fluid flow over a bidirectional stretchable sheet amalgamated with Soret–Dufour effect and chemical reaction is examined by Iftikhar et al.[26]. Significant researches in this direction are mentioned in Refs.[27–38].

Researchers have manifested concern about fluid flow across the permeable surface. The flow through the porous chamber is very common and has widespread applications in industries, petroleum, chemical engineering for instance crude oil extraction, storage of nuclear waste material, movement of oil and water across the oil reservoir, heat exchangers, drying process, MHD generators, seepage of water in river beds, filtration, and water purification process. On a radiative Maxwell nanofluid flow, Jawad et al.[39] analytically investigated the impact of the Soret–Dufour factor on a nonlinear elongated porous surface. Variable characteristics of Newtonian fluid with thermal radiation on a deforming sheet immersed in a porous medium are explored by Megahed et al.[40]. It is reported that on enhancing the viscosity and magnetic parameter, heat flux diminishes. Irfan et al.[41] reported the influence of chemical reaction and internal heat generation/absorption on a radiative bio-nanofluid flow past a deforming surface with stagnation point flow in a porous chamber. On a time-dependent viscous fluid flow, Rosali et al.[42] investigated transmission of heat amalgamated with stagnation point flow past a deforming surface with porosity effect. Substantial research past a permeable deformable surface with several physical aspects is cited in Refs.[43–57].

The aforementioned studies revealed that a good number of studies may be quoted that discuss the nanofluid flow with Soret–Dufour effects past an extended surface. However, the 3D two-phase Casson nanofluid flow amalgamated with dust particles and variable thermal conductivity amalgamated with mass diffusion is still scarce. The impression of the Soret and Dufour effect boosts the transmission of heat and mass. The flow is analyzed numerically with the combined impact of thermal radiation, chemical reaction with activation energy, momentum slip, and convective heat condition. The mathematical model is deciphered through MATLAB software bvp4c. The outcome of numerous parameters is examined via tabular and graphical illustrations. The novelty of the presented mathematical model is illustrated in Table 1 by comparing it with the published studies.

Authors	Soret Dufour effect	3D flow	Dusty fluid	Temperature-dependent thermal conductivity	Thermal radiation	Variable molecular diffusivity	Porous medium	Activation energy
Bibi et al.[4]	No	Yes	Yes	No	Yes	No	No	No
Sohail et al.[10]	No	Yes	No	Yes	Yes	Yes	No	No
Ramadevi et al.[12]	No	Yes	No	Yes	No	No	No	No
Joshi et al.[58]	No	Yes	No	No	No	No	No	No
Ramzan et al.[59]	No	Yes	No	No	No	No	No	Yes
Reddy et al.[60]	Yes	Yes	No	No	Yes	No	No	No
Waqas et al.[61]	No	Yes	No	Yes	Yes	No	No	Yes
Present	Yes	Yes	Yes	Yes	Yes	Yes	Yes	Yes

Table 1. Literature survey for the originality of the presented mode with contemporary published studies.
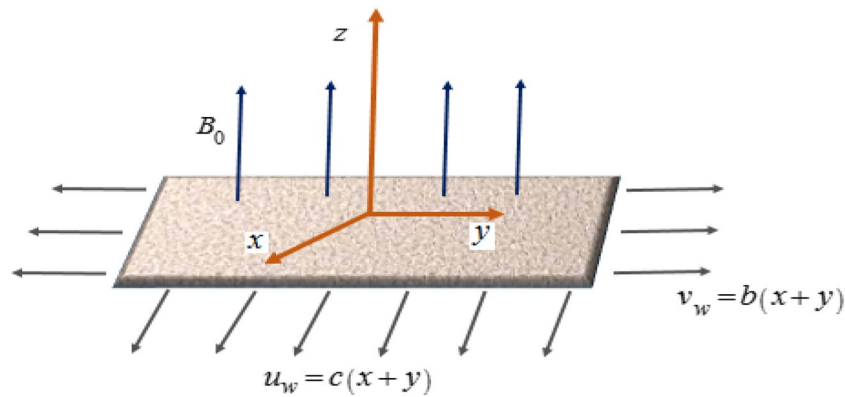
Figure 1. Flow representation of the model.

Formation of the mathematical model

An incompressible, time-independent 3D magnetohydrodynamic dusty radiative Casson nano liquid flow is examined past a deformable surface embedded in a porous medium. The nano-liquid model describes the attributes of Brownian motion and thermophoresis. For the geometry of the problem, a Cartesian coordinate system is considered in such a manner that z-axis is perpendicular to xy − plane. The flow of the subject nanofluid is at the surface $z > 0$ which is generated by a linear bidirectional stretchable surface. The surface is deformable with velocities $u_w = (x + y)c$ and $v_w = (x + y)b$ in the direction of x- and y-axis (Fig. 1). Transfer of heat and mass is enhanced with temperature-dependent thermal conductivity, variable molecular diffusivity incorporated with Soret and Dufour effect. Moreover, the impression of chemical reaction with activation energy and convective heat condition is also analyzed.

For an incompressible flow of Casson fluid extra stress tensor is delineated as[15]:

$$\tau_{ij} = \begin{cases} \left(\mu_c + \dfrac{S_y}{(2\tilde{\pi})^{0.5}}\right)2\tilde{\gamma}_{ij}, & if \ \tilde{\pi} > \tilde{\pi}_c \\ \left(\mu_c + \dfrac{S_y}{(2\tilde{\pi}_c)^{0.5}}\right)2\tilde{\gamma}_{ij}, & if \ \tilde{\pi} < \tilde{\pi}_c, \end{cases} \tag{1}$$

where

$$\begin{aligned} &S_y \text{ is the yield stress of the fluid} \\ &\tilde{\pi} = \tilde{\gamma}_{ij}\tilde{\gamma}_{ij} \text{ is the product of the components of deformation rate} \\ &\tilde{\gamma}_{ij} = \tfrac{1}{2}\left(v_{xi} + v_{yj}\right) \text{ is the rate of the strain tensor} \\ &\tilde{\pi}_c \text{ is the critical value of the product of the components of deformation rate tensor.} \end{aligned} \tag{2}$$

The equations governing the mathematical model with fluid particle suspension[1,23,31,62,63] are:
For fluid flow:

$$\tilde{u}_x + \tilde{v}_y + \tilde{w}_z = 0, \tag{3}$$

$$\tilde{u}\tilde{u}_x + \tilde{v}\tilde{u}_y + \tilde{w}\tilde{u}_z = \nu\left(1 + \frac{1}{\beta}\right)\tilde{u}_{zz} - \frac{\sigma_1 B_0^2}{\rho}\tilde{u} - \frac{\nu}{K^*}\tilde{u} + \frac{KN}{\rho}\left(\tilde{u}_p - \tilde{u}\right), \tag{4}$$

$$\tilde{u}\tilde{v}_x + \tilde{v}\tilde{v}_y + \tilde{w}\tilde{v}_z = \nu\left(1 + \frac{1}{\beta}\right)\tilde{v}_{zz} - \frac{\sigma_1 B_0^2}{\rho}\tilde{v} - \frac{\nu}{K^*}\tilde{v} + \frac{KN}{\rho}\left(\tilde{v}_p - \tilde{v}\right), \tag{5}$$

$$\tilde{u}\tilde{T}_x + \tilde{v}\tilde{T}_y + \tilde{w}\tilde{T}_z = \frac{1}{\rho c_p}\left(k(\tilde{T})\tilde{T}_z\right)_z + \frac{D_T k_t^*}{c_s c_p}\tilde{C}_{zz} + \tau\left(D_B\tilde{C}_z\tilde{T}_z + \frac{D_T}{\tilde{T}_\infty}\left(\tilde{T}_z\right)^2\right)$$
$$- \frac{1}{\rho c_p}q_z(r) + \frac{\rho_p c_p}{(\rho c_p)_f \tau_T}\left(\tilde{T}_P - \tilde{T}\right), \tag{6}$$

$$\tilde{u}\tilde{C}_x + \tilde{v}\tilde{C}_y + \tilde{w}\tilde{C}_y = \left(D_B(\tilde{C})\tilde{C}_z\right)_z + \frac{D_T k_t^*}{\tilde{T}_\infty}\tilde{T}_{zz} + \frac{\rho_p}{\rho\tau_c}\left(C_p - C\right) - k_r^2\left(\frac{\tilde{T}}{\tilde{T}_\infty}\right)^n\left(\tilde{C} - \tilde{C}_\infty\right)\exp\left(\frac{-E_a}{k\tilde{T}}\right). \tag{7}$$

The mathematical form of radiative heat flux[31,64] is as follows:

$$q_r = -\frac{4}{3}\frac{\bar{\sigma}}{\bar{k}}T_z^4, \quad \text{where } T^4 = 4T_\infty^3 T - 3T_\infty^4. \tag{8}$$

In Eq. (6), temperature-dependent thermal conductivity[16,65] is stated as:

$$k(T) = k_\infty\left(1 + d\left(\frac{\tilde{T} - \tilde{T}_\infty}{\tilde{T}_w - \tilde{T}_\infty}\right)\right). \tag{9}$$

In Eq. (7), variable molecular diffusivity[49] is expressed as:

$$D_B(C) = D_{B_\infty}\left(1 + e\left(\frac{\tilde{C} - \tilde{C}_\infty}{\tilde{C}_w - \tilde{C}_\infty}\right)\right). \tag{10}$$

For dusty particle flow:

$$u_x(p) + v_y(p) + w_z(p) = 0, \tag{11}$$

$$u(p)u_x(p) + v(p)u_y + w(p)u_z = \frac{KN}{\rho p}\left(u - u(p)\right), \tag{12}$$

$$u(p)v_x(p) + v(p)v_y + w(p)v_z(p) = \frac{KN}{\rho p}\left(v - v(p)\right), \tag{13}$$

$$u(p)T_x(p) + v(p)T_y(p) + w(p)T_z(p) = \frac{c_p}{c_m\tau_T}\left(T - T(p)\right), \tag{14}$$

$$u(p)C_x(p) + v(p)C_y(p) + w(p)C_z(p) = \frac{mN}{\rho\tau_c}\left(C - C(p)\right), \tag{15}$$

with boundary conditions[1,7,66,67]

$$cc\,\tilde{u}|_{z=0} = c(x + y) + S\left(1 + \frac{1}{\beta}\right)\tilde{u}_z, \quad \tilde{v}|_{z=0} = b(x + y) + S\left(1 + \frac{1}{\beta}\right)\tilde{v}_z,$$
$$\tilde{w}|_{z=0} = 0, \quad -k_f\left(\tilde{T}\right)\tilde{T}_z\Big|_{z=0} = h_1\left(\tilde{T}_w - \tilde{T}\right), \quad \tilde{C}|_{z=0} = \tilde{C}_w,$$
$$u|_{z\to\infty} \to 0, \quad v|_{z\to\infty} \to 0, \quad u_p\big|_{z\to\infty} \to 0, \quad v_p\big|_{z\to\infty} \to 0,$$
$$w_p\big|_{z\to\infty} \to w, \quad T|_{z\to\infty} \to T_\infty, \quad T_p\big|_{z\to\infty} \to T_\infty, \quad C|_{z\to\infty} \to C_\infty, \quad C_p\big|_{z\to\infty} \to C_\infty. \tag{16}$$

Using appropriate subsequent transformation[10]:

$$u = (x + y)cf', \quad v = (x + y)cj', \quad w = -(f + j)\sqrt{cv}, \quad \zeta = \left(\frac{c}{\nu}\right)^{0.5}z, \quad u_p = (x + y)cF',$$
$$v_p = (x + y)cJ', \quad w_p = -(F + J)\sqrt{cv},$$
$$T = (T_w - T_\infty)\theta + T_\infty, \quad T_p = (T_w - T_\infty)\theta_p + T_\infty, \quad C = (C_w - C_\infty)\phi + C_\infty, \quad C_p = (C_w - C_\infty)\phi_p + C_\infty. \tag{17}$$

Equations (3) and (11) are trivially equated. Though Eqs. (4)–(7) and (12)–(15) are transmuted as:
For fluid flow:

$$\left(1 + \frac{1}{\beta}\right)\frac{d^3 f}{d\zeta^3} - \left(\frac{df}{d\zeta}\right)^2 - \frac{dj}{d\zeta}\cdot\frac{df}{d\zeta} + (j+f)\frac{d^2 f}{d\zeta^2} - (Ha + \lambda_1)\frac{df}{d\zeta} + \lambda.\delta_v\left(\frac{dF}{d\zeta} - \frac{df}{d\zeta}\right) = 0, \quad (18)$$

$$\left(1 + \frac{1}{\beta}\right)\frac{d^3 j}{d\zeta^3} - \left(\frac{dj}{d\zeta}\right)^2 - \frac{dj}{d\zeta}\cdot\frac{df}{d\zeta} + (j+f)\frac{d^2 j}{d\zeta^2} - (Ha + \lambda_1)\frac{dj}{d\zeta} + \lambda.\delta_v\left(\frac{dJ}{d\zeta} - \frac{dj}{d\zeta}\right) = 0, \quad (19)$$

$$\left((1 + d\theta) + \frac{4}{3}Rd\right)\frac{d^2\theta}{d\zeta^2} + d\left(\frac{d\theta}{d\zeta}\right)^2 + \Pr\left(\begin{array}{c}(f+j)\frac{d\theta}{d\zeta} + D_f\frac{d^2\phi}{d\zeta^2} + N_b\frac{d\theta}{d\zeta}\frac{d\phi}{d\zeta} \\ + N_t\left(\frac{d\theta}{d\zeta}\right)^2 + \lambda\delta_T(\theta_p - \theta)\end{array}\right) = 0, \quad (20)$$

$$(1 + e\phi)\frac{d^2\phi}{d\zeta^2} + e\left(\frac{d\phi}{d\zeta}\right)^2 + S_c\left(\begin{array}{c}(f+j)\frac{d\phi}{d\zeta} + \lambda\delta_c(\phi_p - \phi) + S_r\frac{d^2\theta}{d\zeta^2} \\ -\delta\phi(1+\alpha\theta)^n \exp\left(\frac{-E}{1+\alpha\theta}\right)\end{array}\right) = 0. \quad (21)$$

For the dusty flow:

$$(J + F)\frac{d^2 F}{d\zeta^2} - \left(\frac{dF}{d\zeta}\right)^2 - \frac{dJ}{d\zeta}\cdot\frac{dF}{d\zeta} + \delta_v\left(\frac{df}{d\zeta} - \frac{dF}{d\zeta}\right) = 0, \quad (22)$$

$$(J + F)\frac{d^2 J}{d\zeta^2} - \left(\frac{dJ}{d\zeta}\right)^2 - \frac{dJ}{d\zeta}\cdot\frac{dF}{d\zeta} + \delta_v\left(\frac{dj}{d\zeta} - \frac{dJ}{d\zeta}\right) = 0, \quad (23)$$

$$(J + F)\frac{d\theta_p}{d\zeta} + \gamma\delta_T(\theta - \theta_p) = 0, \quad (24)$$

$$(F + J)\frac{d\phi_p}{d\zeta} + \lambda.\delta_c(\phi - \phi_p) = 0, \quad (25)$$

and the boundary conditions take the form:

$$f(\zeta) = 0, \, j(\zeta) = 0, \, \frac{df}{d\zeta} = 1 + L\left(1 + \frac{1}{\beta}\right)\frac{d^2 f}{d\zeta^2}, \, \frac{dj}{d\zeta} = P + L\left(1 + \frac{1}{\beta}\right)\frac{d^2 j}{d\zeta^2},$$

$$\frac{d\theta}{d\zeta} = -H_1\left(\frac{1 - \theta(0)}{1 + d\theta}\right), \phi(\zeta) = 1 \quad \text{at } \zeta = 0,$$

$$\frac{df}{d\zeta} \to 0, \frac{dj}{d\zeta} \to 0, \frac{dF}{d\zeta} \to 0, \frac{dJ}{d\zeta} \to 0, F(\zeta) \to f(\zeta),$$

$$J(\zeta) \to j(\zeta), \theta(\zeta) \to 0, \theta_p(\zeta) \to 0, \phi(\zeta) \to 0, \, \phi_p(\zeta) \to 0 \quad \text{as } \zeta \to \infty. \quad (26)$$

The mathematical forms of shear stress at the wall (drag force coefficient), local Nusselt, and Sherwood number are specified as:

$$C_{f_x} = \frac{\tau(zx)|_{z=0}}{\rho u_w^2}, \, \tau(zx) = \mu\left(1 + \frac{1}{\beta}\right)u_z, \quad (27)$$

$$C_{j_y} = \frac{\tau(zy)\big|_{z=0}}{\rho u_w^2}, \, \tau(zy) = \mu\left(1 + \frac{1}{\beta}\right)v_z, \quad (28)$$

$$Nu(x) = \frac{xQ_w}{k_\infty\left(\tilde{T}_w - \tilde{T}_\infty\right)}, \, Q_w = -k(T)T_z + q(r)\big|_{z=0}, \quad (29)$$

$$Sh(x) = \frac{xQ_m}{D_{B_\infty}(C_w - C_\infty)}, \, Q_m = -D_B(C)\,C_z|_{z=0}. \quad (30)$$

By employing Eq. (17), the dimensionless form of Eqs. (27)–(30) are as follow:

$$(\mathrm{Re}_x)^{0.5} C_{f_x} = \left(1 + \frac{1}{\beta}\right) \frac{d^2 f}{d\zeta^2}\bigg|_{\zeta=0}, \tag{31}$$

$$(\mathrm{Re}_x)^{0.5} C_{j_y} = \left(1 + \frac{1}{\beta}\right) \frac{d^2 j}{d\zeta^2}\bigg|_{\zeta=0}, \tag{32}$$

$$Nu(x)(\mathrm{Re}_x)^{-0.5} = -\left(1 + \frac{4}{3}\left(\frac{Rd}{1 + d\theta}\right)\right) \frac{d\theta}{d\zeta}\bigg|_{\zeta=0}, \tag{33}$$

$$Sh(x)(\mathrm{Re}_x)^{-0.5} = -\frac{1}{(1 + e\phi(\zeta))} \frac{d\phi}{d\zeta}\bigg|_{\zeta=0}. \tag{34}$$

Numerical procedure

The coupled nonlinear ODEs are computed numerically by employing the bvp4c function in MATLAB. Mentioned numerical code is used, we obtain ODEs which are of order one.

$$f = Y_1, f' = Y_2, f'' = Y_3, f''' = Y_3' = YY_1, F = Y_4, F' = Y_5, F'' = Y_5' = YY_2,$$

$$j = Y_6, j' = Y_7, j'' = Y_8, j' = Y_8' = YY_3, J = Y_9, J' = Y_{10}, J'' = Y_{10}' = YY_4,$$

$$YY_1 = \frac{1}{\left(1 + \frac{1}{\beta}\right)} \left(Y_2^2 + Y_7 \cdot Y_2 - (Y_1 + Y_6)Y_3 + (Ha + \lambda_1)Y_2 - \lambda \cdot \delta_\nu(Y_5 - Y_2)\right),$$

$$YY_2 = \frac{1}{(Y_9 + Y_4)} \left(Y_5^2 + Y_{10} \cdot Y_5 - \delta_\nu(Y_2 - Y_5)\right),$$

$$YY_3 = \frac{1}{\left(1 + \frac{1}{\beta}\right)} \left(Y_7^2 + Y_7 \cdot Y_2 - (Y_6 + Y_1)Y_8 + (Ha + \lambda_1)Y_7 - \lambda \cdot \delta_\nu(Y_{10} - Y_7)\right),$$

$$YY_4 = \frac{1}{(Y_9 + Y_4)} \left(Y_{10}^2 + Y_{10} \cdot Y_5 - \delta_\nu(Y_7 - Y_{10})\right),$$

$$\theta = Y_{11}, \theta' = Y_{12}, \theta'' = Y_{12}' = YY_5, \theta_p = Y_{13}, \theta_p' = Y_{13}' = YY_6,$$

$$\phi = Y_{14}, \phi = Y_{15}, \phi'' = Y_{15}' = YY_7,$$

$$\phi_p = Y_{16}, \phi_p' = Y_{16}' = YY_8.$$

$$YY_8 = \frac{1}{(Y_9 + Y_4)} (\lambda \cdot \delta_c(Y_{16} - Y_{14}))$$

$$YY_5 = \frac{1}{\left((1 + d \cdot Y_{11}) + \frac{4}{3}Rd\right)} \left(-d \cdot Y_{12}^2 - \mathrm{Pr}\left(\begin{array}{c}(Y_1 + Y_6)Y_{12} + D_f.YY_7 + N_b \cdot Y_{12} \cdot Y_{15} \\ +N_t \cdot Y_{12}^2 + \lambda \cdot \delta_T(Y_{13} - Y_{11})\end{array}\right)\right),$$

$$YY_6 = \frac{1}{(Y_9 + Y_4)} (-\gamma \cdot \delta_T(Y_{11} - Y_{13})),$$

$$YY_7 = \frac{1}{(1 + e \cdot Y_{14})} \left(-e \cdot Y_{15}^2 + S_c \left(\begin{array}{c}\delta \cdot Y_{14}(1 + \alpha \cdot Y_{11})^n \exp\left(\frac{-E}{1 + \alpha \cdot Y_{11}}\right) \\ -(Y_1 + Y_6)Y_{15} - S_r \cdot YY_5 - \lambda \cdot \delta_c(Y_{16} - Y_{14})\end{array}\right)\right),$$

and the boundary conditions are enumerated as

$$Y_1(0) = 0, Y_6(0) = 0, Y_2(0) = 1 + L \cdot \left(1 + \frac{1}{\beta}\right) Y_3(0), Y_7(0) = P + L \cdot \left(1 + \frac{1}{\beta}\right) Y_8(0),$$

$$Y_{12}(0) = -H_1\left(\frac{(1 - Y_{11}(0))}{1 + d \cdot Y_{11}(0)}\right), Y_{14}(0) = 1 \quad \text{At } \zeta = 0 \tag{35}$$

$$Y_2(\infty) \to 0, Y_7(\infty) \to 0, Y_5(\infty) \to 0, Y_{10}(\infty) \to 0, Y_4(\infty) \to Y_1(\infty),$$

$$Y_9(\infty) \to Y_6(\infty), Y_{11}(\infty) \to 0, Y_{13}(\infty) \to 0, Y_{14}(\infty) \to 0, Y_{16}(\infty) \to 0. \quad \text{As } \zeta \to \infty.$$

Analysis of results

For the graphical analysis of the dimensionless parameters versus involved profiles appearing in the highly nonlinear mathematical problem in Eqs. (18)–(25). This problem is elucidated numerically by utilizing bvp4c, an implemented function in MATLAB. Figures 2, 3, 4, 5 demonstrate the influence of Casson fluid parameter β, porosity parameter λ_1, velocity slip parameter L, and fluid-particle interaction parameter δ_ν on the velocity of the fluid $f'(\zeta), j'(\zeta)$ (in x and y direction) and dust phase $F'(\zeta)$ and $J'(\zeta)$. The aftermath of β on velocity field for both phases is illustrated in Fig. 2a–d. These figures depict that β is inversely proportional to yield stress S_y.
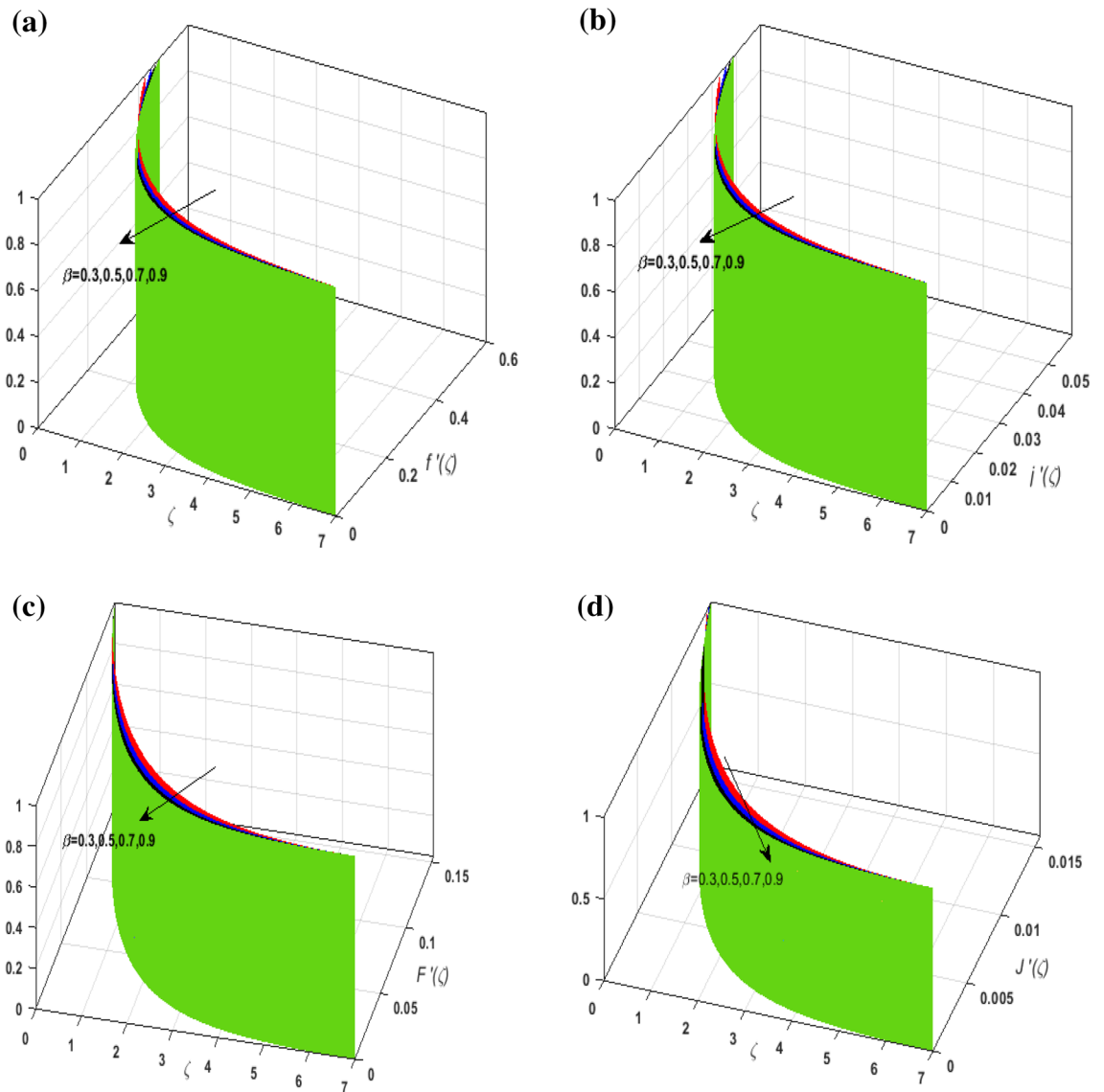
Figure 2. (**a**) Upshot of β on $f'(\zeta)$. (**b**) Upshot of β on $j'(\zeta)$. (**c**) Upshot of β on $F'(\zeta)$. (**d**) Upshot of β on $J'(\zeta)$.

It is found that on escalating β yield stress decreases. This generates a resistive force that causes hindrance to the fluid flow. Consequently, both phases deteriorate as β escalate. The effect of the porosity parameter λ_1 on fluid and dust phase is illustrated in Fig. 3a–d. Since λ_1 is the quotient of kinematic viscosity to the permeability of the porous medium. Growing values of λ_1 escalates the kinematic viscosity of the fluid. This accelerates the resistance in the system. It is witnessed that rising values of λ_1 results in deterrence to the motion of the fluid. Therefore, the velocity field for both phases diminishes. Figure 4a–d are sketched to depict the impact of slip parameters L on both phases. It is found that growing values of H_1 strengthens the friction force. This causes more liquid to slip past the deformable bidirectional surface. Thus, the fluid flow depreciates for both phases. The impression of δ_v on both phases is illustrated in Fig. 5a–d. It is observed that for rising values of δ_v relaxation time of suspended particles decays. Dusty granules generate a force that will resist the flow. Therefore, fluid velocity depreciates on mounting δ_v, however, an opposite upshot is perceived for dusty flow. Figures 6, 7, 8, 9, 10, 11, 12 depict the outcome of sundry parameters on the temperature field of fluid and dusty granules i.e., $\theta(\zeta)$ and $\theta_p(\zeta)$. The outcome of the radiation parameter Rd on $\theta(\zeta)$ and $\theta_p(\zeta)$ is discussed in Fig. 6a,b. Since $Rd = \frac{4\bar{\sigma} T_\infty^3}{3\bar{k} k}$, so by up surging Rd the mean absorption coefficient decreases. It is perceived that on escalating Rd additional heat is produced in the system. Therefore, due to growing values of Rd more heat is transmitted to the fluid. Hence, $\theta(\zeta)$ and $\theta_p(\zeta)$ rise for suspended particle and fluid phase. Figure 7a,b is sketched to analyze the behavior of heat transfer Biot number H_1 on $\theta(\zeta)$ and $\theta_p(\zeta)$. For growing values of H_1 heat transfer coefficient intensifies. On elevating H_1 fluid flow accelerates. Thus, $\theta(\zeta)$ and $\theta_p(\zeta)$ escalates on augmenting H_1. The performance of the thermal conductivity parameter d on $\theta(\zeta)$ and $\theta_p(\zeta)$ is addressed in Fig. 8a,b. On accelerating d temperature-dependent thermal conductivity amplifies. It is seen that rising values of d, results in an amplified collision among the particles. This leads to more exchange of heat through the fluid. Thus, $\theta(\zeta)$ and $\theta_p(\zeta)$ elevates on augmenting d for both phases. Consequently, thicker penetration depth increases due to convective heat transfer at the surface. Figure 9a,b
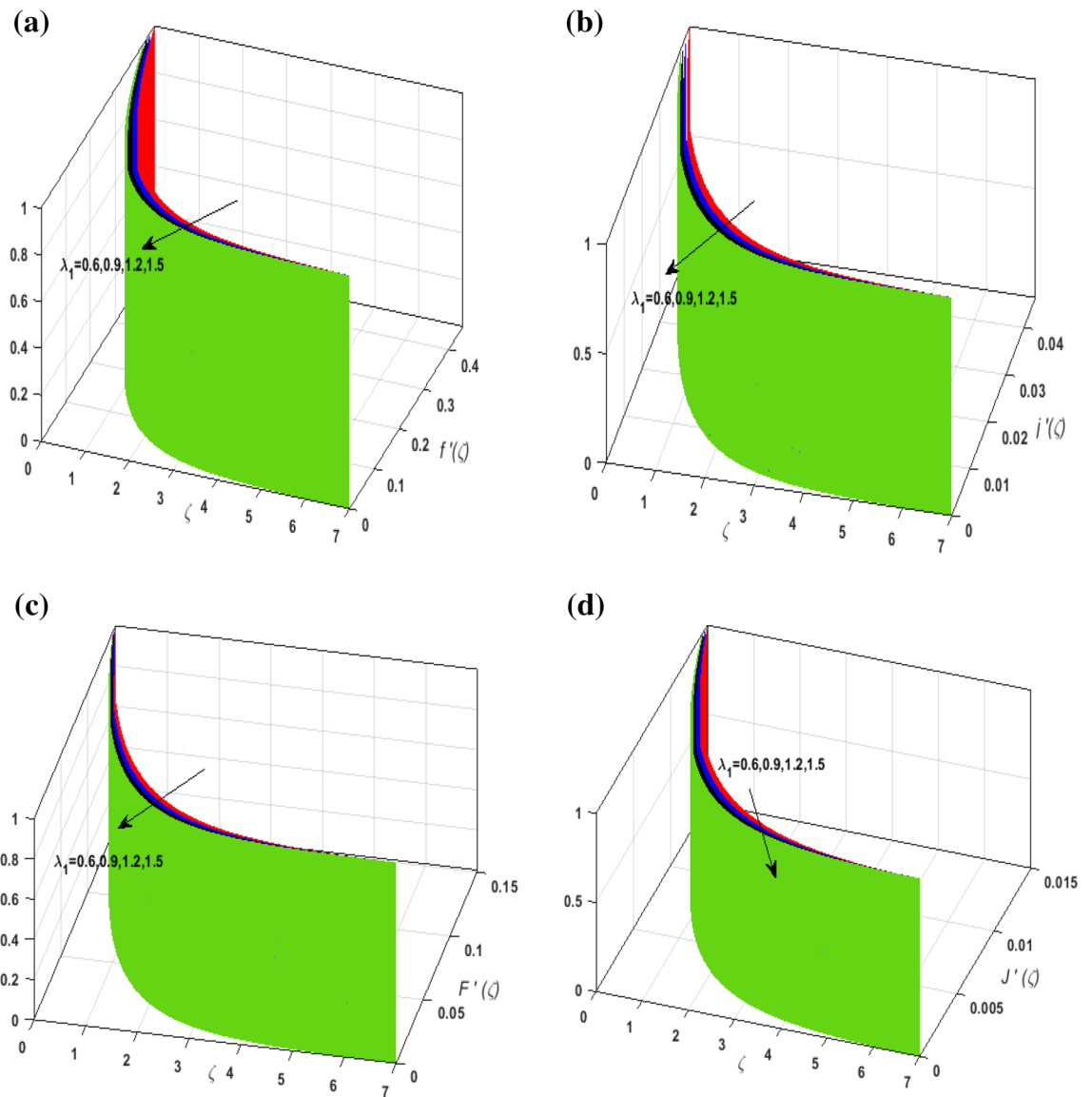
Figure 3. (**a**) Upshot of λ_1 on $f'(\zeta)$. (**b**) Upshot of λ_1 on $j'(\zeta)$. (**c**) Upshot of λ_1 on $F'(\zeta)$. (**d**) Upshot of λ_1 on $J'(\zeta)$.

illustrate the fluctuation in fluid-particle interaction parameter δ_r for both phases $\theta(\zeta)$ and $\theta_p(\zeta)$. It is witnessed that on incrementing δ_r fluid flow slows down. This corresponds to a decline in fluid flow. However, growing values of δ_r in suspended particles strengthen the frictional force. Hence, a reverse trend is observed for $\theta_p(\zeta)$. The impact of thermophoresis parameter N_t on $\theta(\zeta)$ and $\theta_p(\zeta)$ is displayed in Fig. 10a,b. It is observed that on enhancing N_t, thermophoretic force is strengthened. As a result, fluid particles move from hot to cold fluid. Thus, $\theta(\zeta)$ and $\theta_p(\zeta)$ augment. Figure 11a,b illustrate the impression of the Brownian motion parameter N_b on $\theta(\zeta)$ and $\theta_p(\zeta)$. For growing values of N_b collision among the fluid particles increases due to which more heat is generated. Therefore, $\theta(\zeta)$ and $\theta_p(\zeta)$ rises. To understand the variation of Dufour number D_f on $\theta(\zeta)$ and $\theta_p(\zeta)$ Fig. 12a,b is plotted. On escalating D_f concentration gradient enhances which results in heat transmission. Thus, a prominent upsurge is found in the thermal state of $\theta(\zeta)$ and $\theta_p(\zeta)$. The impression of varying Schmidt number S_c on the concentration field $\phi(\zeta)$ is discussed in Fig. 13. As S_c is the quotient of kinematic viscosity ν to Brownian diffusion coefficient D_B. It is observed that rising values of S_c diminishes the Brownian motion parameter. Thus, mass diffusion reduces for growing values of S_c. This results in the reduction of the concentration of the fluid. Therefore, deteriorating nature is exhibited by $\phi(\zeta)$ on boosting S_c. Figure 14 is drawn to elucidate the upshot of dimensionless chemical reaction parameter δ on $\phi(\zeta)$. On up surging δ chemical molecular diffusivity reduces owing to its consumption in the reaction. A slight decrement is observed in the boundary layer thickness. Thus, the concentration of the fluid deteriorates. The influence of variable molecular diffusivity e on $\phi(\zeta)$ is exhibited in Fig. 15. Since e is proportionate to $\phi(\zeta)$. For mounting values of e variable mass diffusion elevates. Consequently, $\phi(\zeta)$ augments. The impact of rising values of activation energy E is deliberated in Fig. 16. It is noticed that escalating values of E lead to a decrease in the Arrhenius function. Consequently, the generative chemical reaction decelerates. Thus, on accelerating E, the fluid concentration upsurges. Figure 17 is sketched to analyze the effect
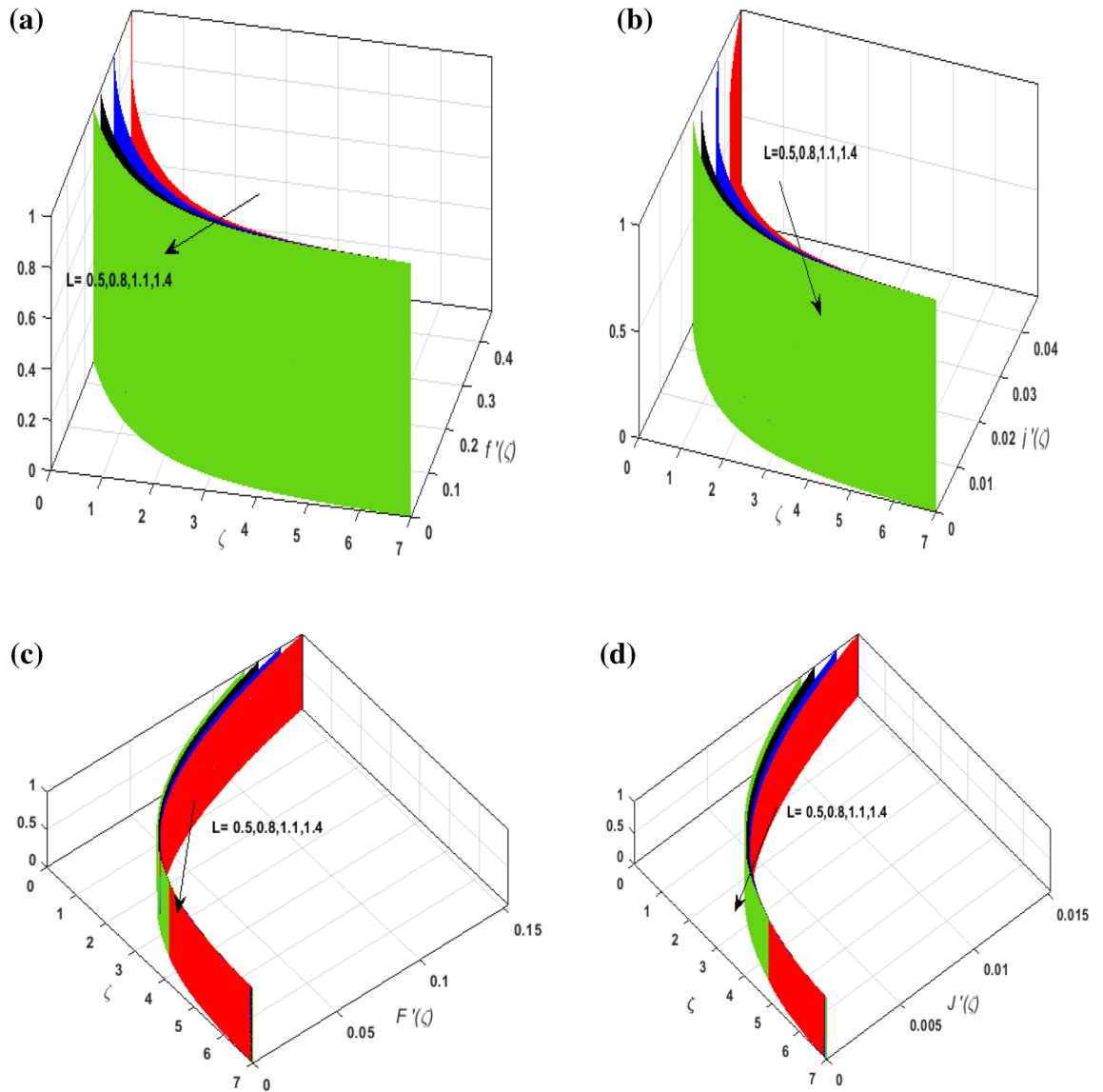
Figure 4. (**a**) Upshot of L on $f'(\zeta)$. (**b**) Upshot of L on $j'(\zeta)$. (**c**) Upshot of L on $F'(\zeta)$. (**d**) Upshot of L on $J'(\zeta)$.

of Soret number S_r on $\phi(\zeta)$. S_r is the quotient of difference in temperature and concentration. On escalating S_r, the temperature gradient rises. It is perceived that molecular diffusion increases. Thus, the rate of mass transfer intensifies for growing values of S_r. Consequently, $\phi(\zeta)$ enhances.

The outcome of tabulated values of dimensionless parameters λ_1, H_a, δ, and L on drag force coefficient is depicted in Table 2. It is perceived that on escalating λ_1, H_a, and δ. shear stress increases. The influence of $Pr, Rd, D_f, N_b, S_c, \delta, S_r$, and δ_T on local Nusselt number and Sherwood number is portrayed in Table 3. It is perceived that on escalating Rd heat and mass flux both augments. For growing values of D_f, N_b, S_c, and δ heat flux diminishes, whereas, mass flux upsurges. A deteriorating nature is exhibited by mass transfer on amplifying S_r and δ_r, however, the rate of heat transfer amplifies. A comparative analysis of the present investigation is exhibited in Table 4 with Wang[68]. A good association between the results is seen.

Concluding remarks

Numerical solution for dusty radiative Casson nanofluid flow with temperature-dependent thermal conductivity and variable molecular mass diffusion has been investigated past a deformable bidirectional surface. Transfer of heat and mass is enhanced by inspecting the impression of the Soret–Dufour factor amalgamated with chemical reaction and activation energy. The flow is incorporated with additional effects of momentum slip and convective
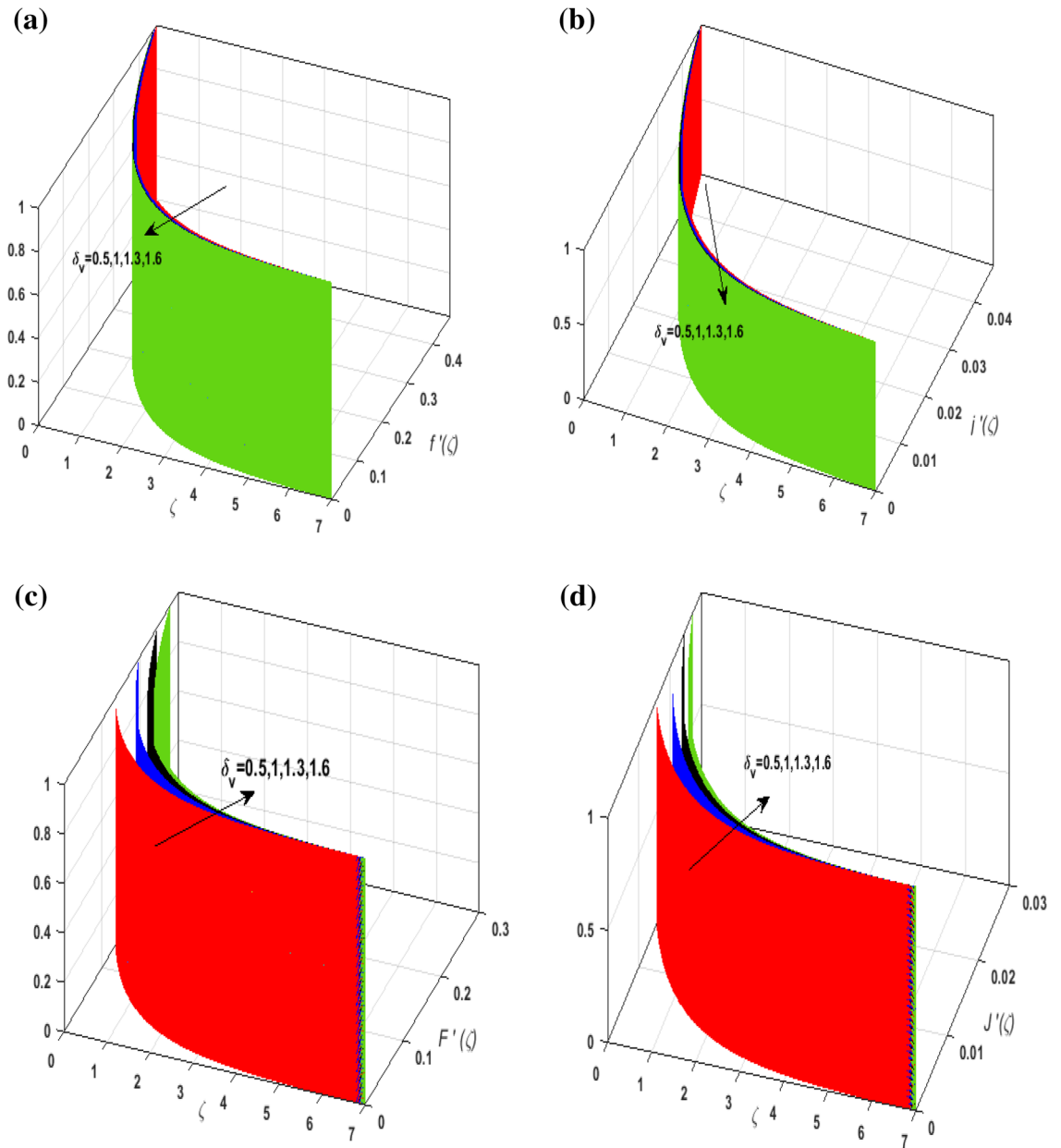
Figure 5. (**a**) Upshot of L on $f'(\zeta)$. (**b**) Upshot of L on $j'(\zeta)$. (**c**) Upshot of L on $F'(\zeta)$. (**d**) Upshot of L on $J'(\zeta)$.

heat conditions. The mathematical model is deciphered through bvp4c, an implemented function in MATLAB. The perceptible analyses of the present exploration are:

- For growing values of β, λ_1, and L velocity field declines for fluid-particle suspension.
- A reverse trend is noticed in the velocity field for enhancing δ_v for both phases.
- An increasing behavior is exhibited by the thermal field for growing values of Rd, H_1, D_f and N_t for fluid and dust phase.
- An opposite behavior is noticed in the thermal field for fluctuation in fluid-particle interaction parameters for the fluid and dust phase.
- For larger values of S_c, and δ, the concentration field declines.
- The concentration field augments on amplifying E and S.
- Drag force coefficient increases on escalating λ_1, H_a, and δ_v.
- The mass transfer exhibits a deteriorating impact on amplifying S_r, and δ_r, however, the rate of heat transfer amplifies.
- Heat and mass flux augments on escalating $RdRd$.

(a)

(b)
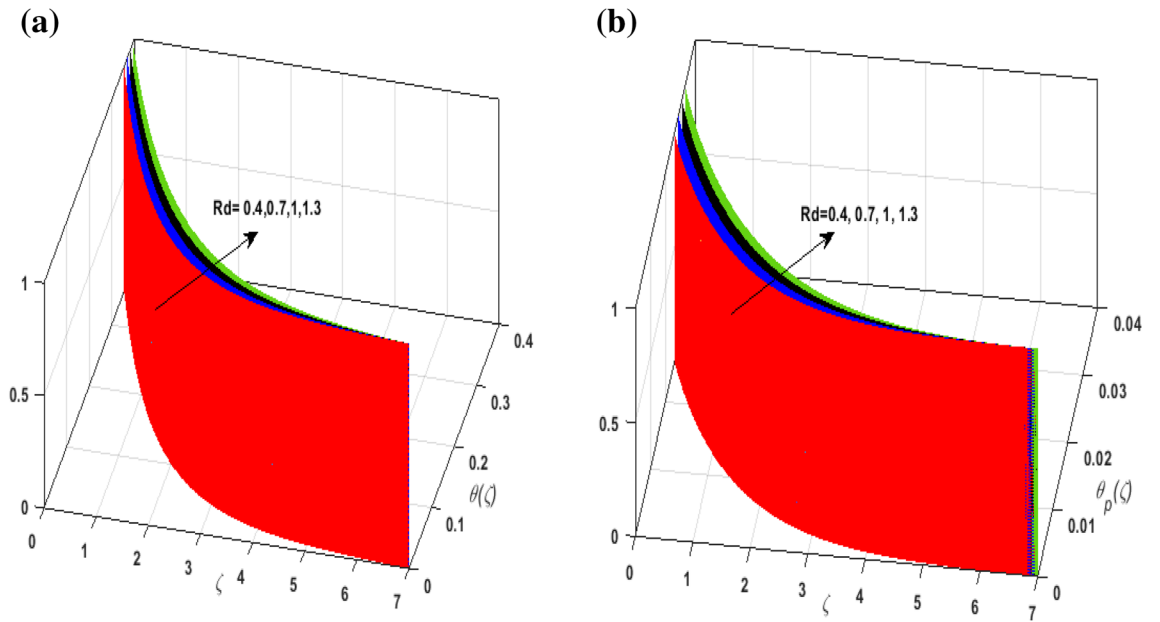
Figure 6. (**a**) Upshot of Rd on $\theta(\zeta)$. (**b**) Upshot of Rd on $\theta_p(\zeta)$.
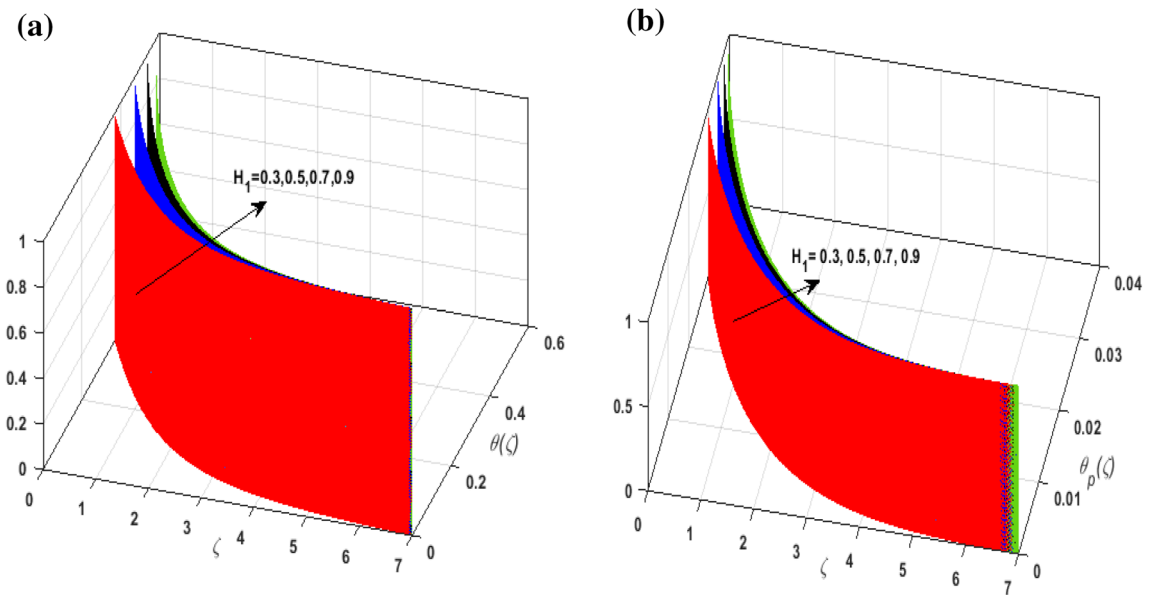
(a)

(b)

Figure 7. (**a**) Upshot of H_1 on $\theta(\zeta)$. (**b**) Upshot of H_1 on $\theta_p(\zeta)$.
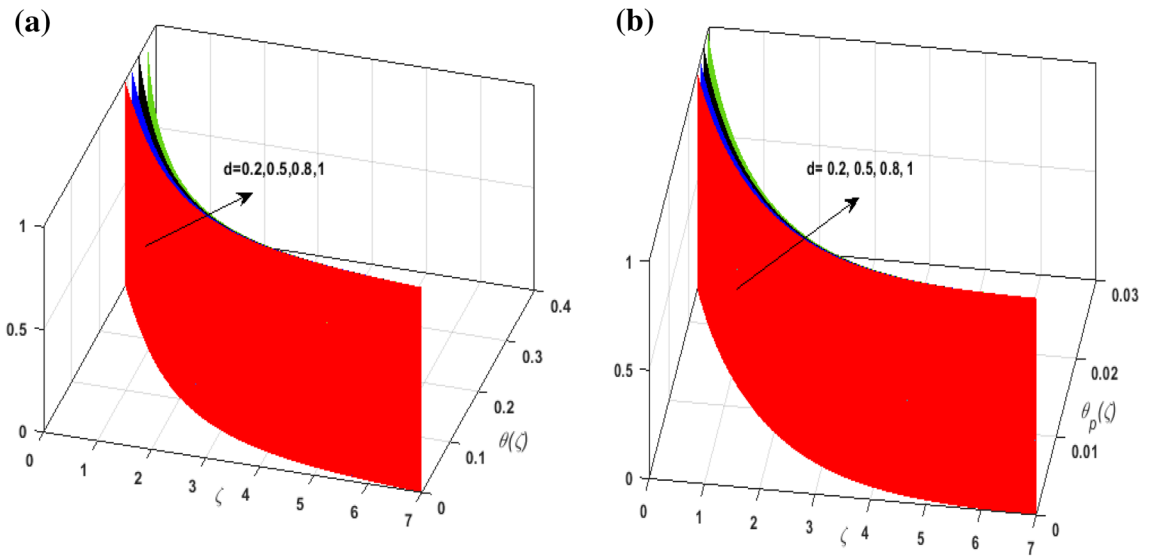
Figure 8. (**a**) Upshot of d on $\theta(\zeta)$. (**b**) Upshot of d on $\theta_p(\zeta)$.
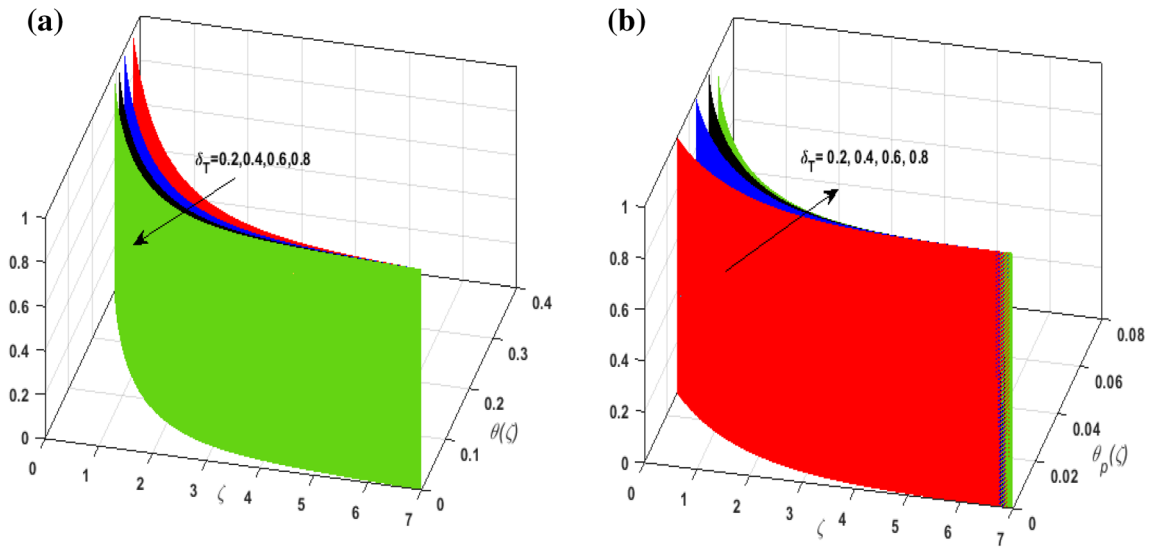

Figure 9. (**a**) Upshot of δ_T on $\theta(\zeta)$. (**b**) Upshot of δ_T on $\theta_p(\zeta)$.

13

(a)

(b)
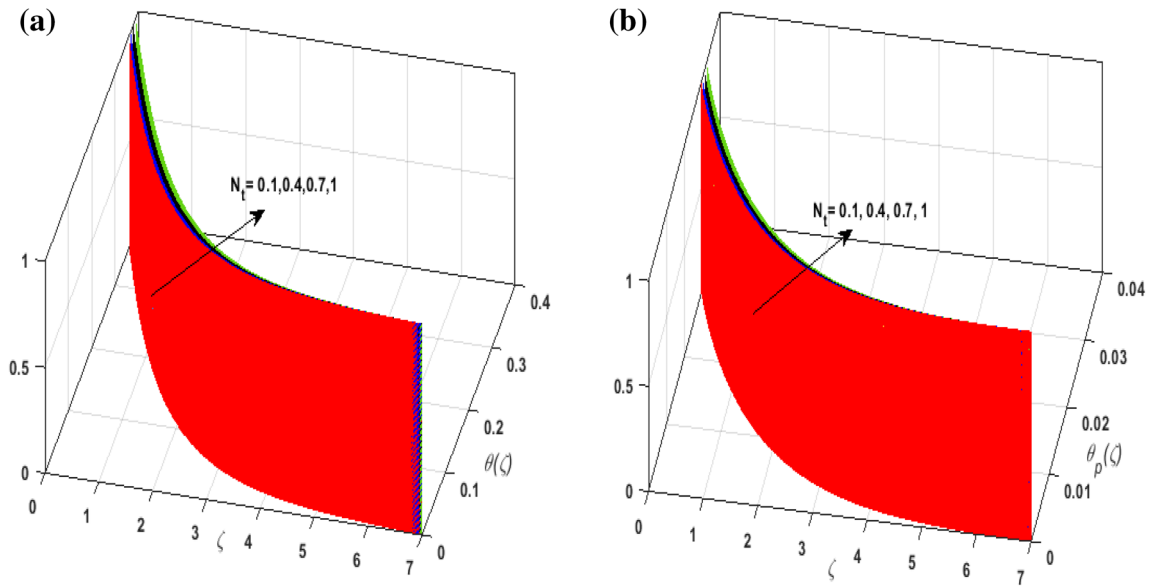
Figure 10. (**a**) Upshot of N_t on $\theta(\zeta)$. (**b**) Upshot of N_t on $\theta_p(\zeta)$.

(a)

(b)
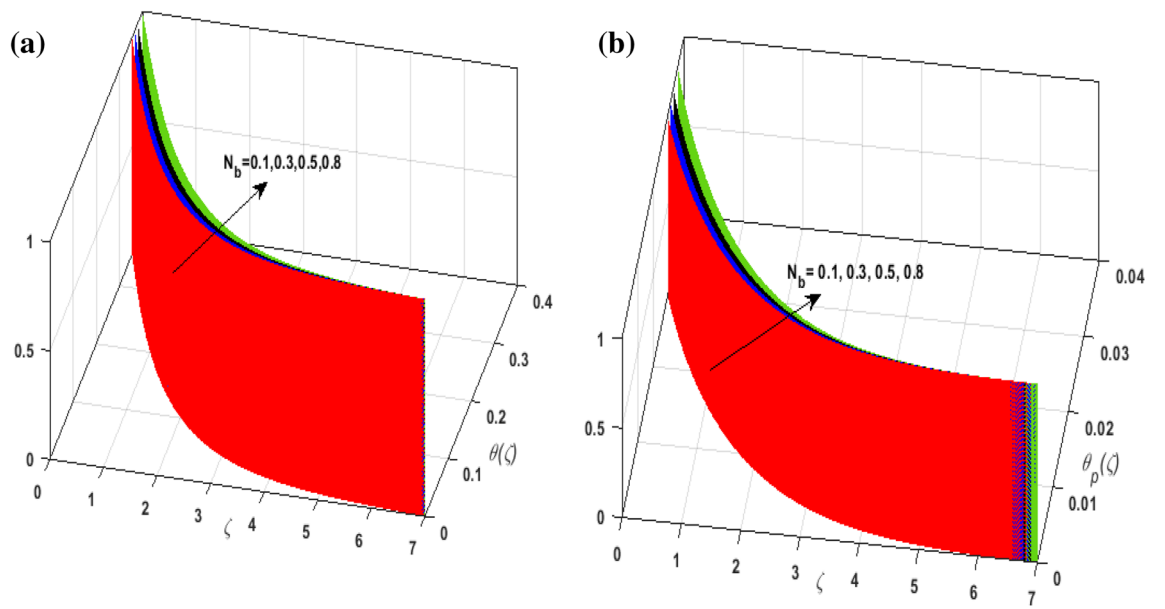
Figure 11. (**a**) Upshot of N_b on $\theta(\zeta)$. (**b**) Upshot of N_b on $\theta_p(\zeta)$.

(a)

(b)
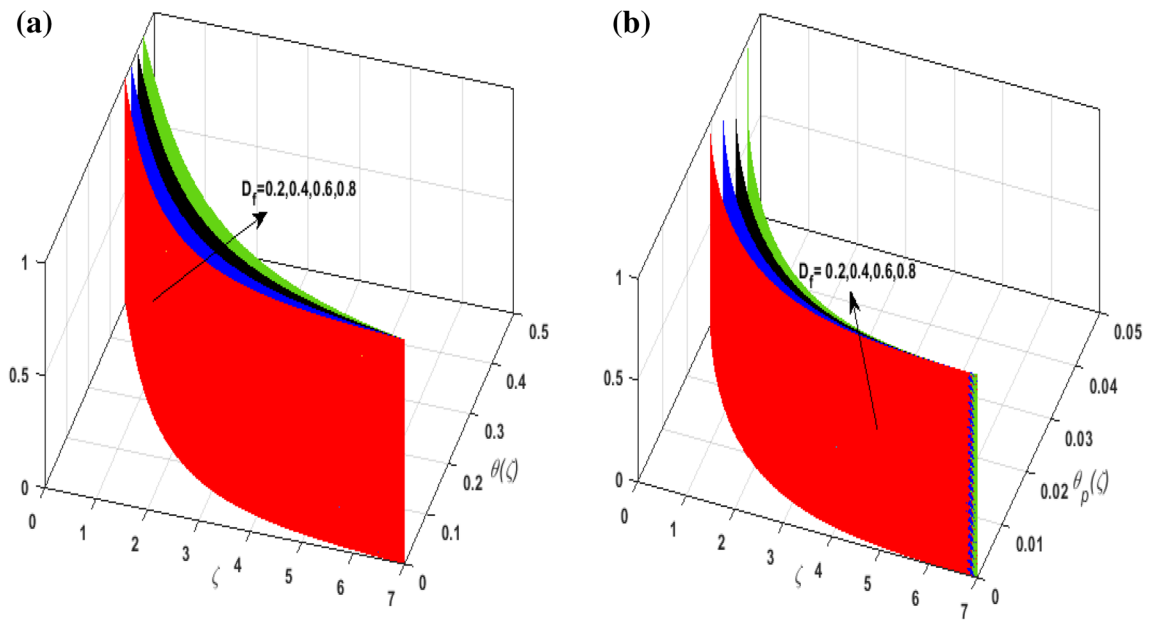
Figure 12. (**a**) Upshot of D_f on $\theta(\zeta)$. (**b**) Upshot of D_f on $\theta_p(\zeta)$.
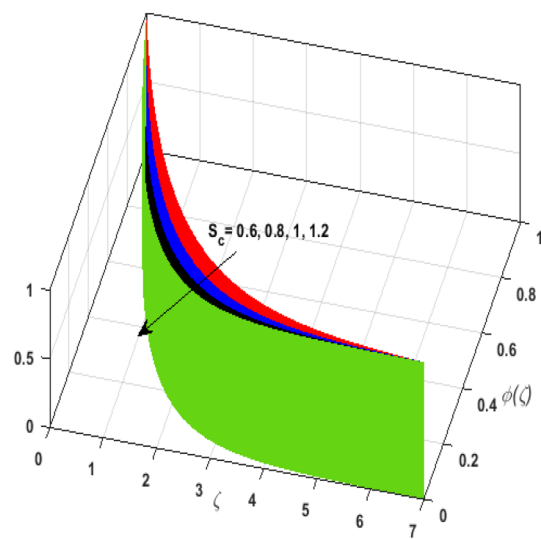
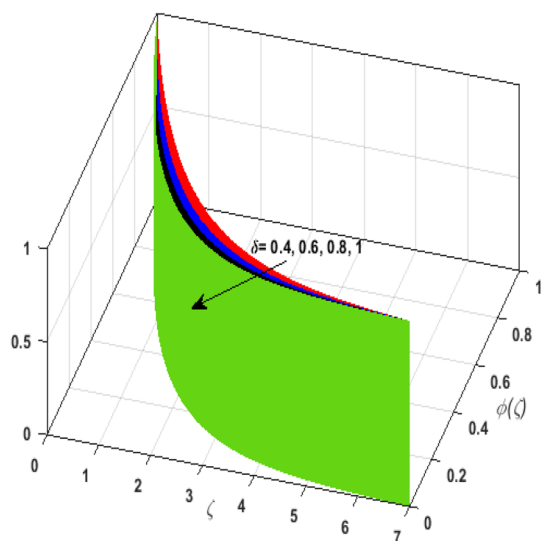**Figure 13.** Upshot of S_c on $\phi(\zeta)$.
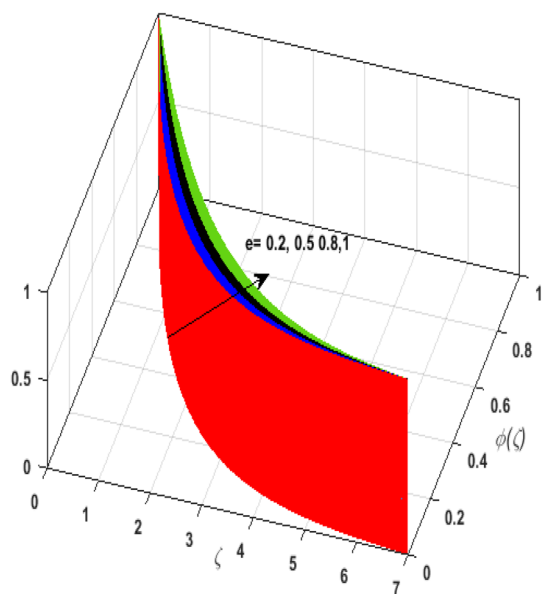
Figure 14. Upshot of δ on $\phi(\zeta)$.

Figure 15. Upshot of e on $\phi(\zeta)$.
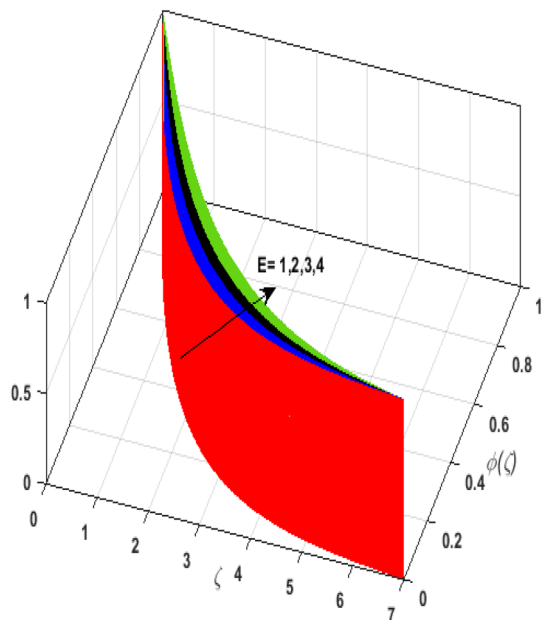
Figure 16. Upshot of E on $\phi(\zeta)$.
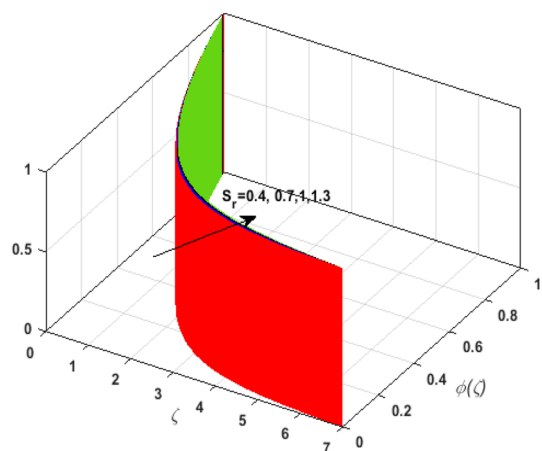
Figure 17. Upshot of S_r on $\phi(\zeta)$.

λ_1	Ha	δ_v	L	$-(\text{Re}_x)^{0.5}C_{f_x}$	$-(\text{Re}_x)^{0.5}C_{f_y}$
0.5				1.0587562	0.10587562
0.6				1.0719469	0.10719469
0.7				1.0845045	0.10845045
	0.3			0.98104151	0.098104151
	0.4			0.99841054	0.099841055
	0.5			1.0147795	0.10147795
		0.3		1.0060463	0.10060463
		0.5		1.0147795	0.10147795
		0.7		1.0213022	0.10213022
			0.4	1.1423770	0.1142377
			0.5	1.0147795	0.10147795
			0.6	0.9139351	0.09139351

Table 2. Computational values of friction drag coefficient for distinct values of λ_1, Ha, L and L.

Pr	Rd	D_f	N_b	S_c	δ	S_r	δ_T	$Nu_x(\mathrm{Re}_x)^{-0.5}$	$Sh_x(\mathrm{Re}_x)^{-0.5}$
3								0.26287551	0.27159206
5								0.28311948	0.26845204
7								0.2946139	0.26679483
	0.3							0.24448878	0.27460726
	0.6							0.29656071	0.27649881
	0.9							0.34511853	0.27805908
		0.3						0.22529783	0.39278698
		0.5						0.20025387	0.39816084
		0.7						0.17477315	0.40337968
			0.2					0.24141581	0.27734281
			0.5					0.23190415	0.27863757
			0.7					0.2253281	0.27953848
				0.6				0.20919744	0.49599463
				0.8				0.19513655	0.58476006
				1.2				0.17110717	0.73964817
					0.4			0.23334648	0.34198783
					0.6			0.22529783	0.39540692
					0.8			0.21795961	0.44369725
						0.4		0.17026475	0.42250068
						0.6		0.17169455	0.41714266
						0.8		0.17319573	0.41215419
							0.3	0.22529789	0.42526637
							0.6	0.25082223	0.41921075
							0.9	0.26650763	0.41543192

Table 3. Computational values of $Nu_x\mathrm{Re}_x^{-0.5}$ and $Sh_x\mathrm{Re}_x^{-0.5}$ against different estimation of $Pr, Rd, D_f, N_b, S_c, \delta, S_r$ and δ_T.

P	$f''(0)$		$j''(0)$		$f(\infty)$		$j(\infty)$	
	[68]	Present	[68]	Present	[68]	Present	[68]	Present
0	− 1	− 1	0	0	1	1	0	0
0.25	− 1.048813	− 1.048762	− 0.194564	− 0.194534	0.907075	0.907052	0.257986	0.257974
0.5	− 1.093097	− 1.093092	− 0.465205	− 0.465127	0.842360	0.842325	0.451671	0.451635
0.75	− 1.134485	− 1.134453	− 0.794622	− 0.794612	0.792308	0.792353	0.612049	0.612026
1	− 1.173720	− 1.173628	− 1.173720	− 1.173724	0.751527	0.751516	0.751527	0.751525

Table 4. Comparison of $f''(0), j''(0), f(\infty)$ and $j(\infty)$ for numeric values of P with Wang[68].

References

1. Hady, F. M., Mahdy, A., Mohamed, R. A. & Zaid, O. A. A. Modeling non-Darcy natural convection flow of a micropolar dusty fluid with convective boundary condition. *Int. J. Aerosp. Mech. Eng.* **14**(2), 41–47 (2020).
2. Zokri, S. M., Arifin, N. S., Kasim, A. R. M., Salleh, M. Z. & Arifin, N. A. N. Jeffrey fluid embedded with dust particles over a shrinking sheet: A numerical investigation. *J. Adv. Res. Fluid Mech. Therm. Sci.* **74**(2), 196–209 (2020).
3. Dey, D., & Chutia, B. Dusty nanofluid flow with bioconvection past a vertical stretching surface. *J. King Saud Univ. Eng. Sci.* https://doi.org/10.1016/j.jksues.2020.11.001 (2020).
4. Bibi, M., Zeeshan, A. & Malik, M. Y. Numerical analysis of unsteady flow of three-dimensional Williamson fluid-particle suspension with MHD and nonlinear thermal radiations. *Eur. Phys. J. Plus* **135**(10), 1–26 (2020).
5. Reddy, M. G., Rani, M. S., Kumar, K. G., Prasannakumar, B. C. & Lokesh, H. J. Hybrid dusty fluid flow through a Cattaneo–Christov heat flux model. *Phys. A Stat. Mech. Appl.* **551**, 123975 (2020).
6. Reddy, M. G. & Ferdows, M. Species and thermal radiation on micropolar hydromagnetic dusty fluid flow across a paraboloid revolution. *J. Therm. Anal. Calorim.* **143**, 1–19 (2020).
7. Souayeh, B. *et al.* Slip flow and radiative heat transfer behavior of Titanium alloy and ferromagnetic nanoparticles along with suspension of dusty fluid. *J. Mol. Liq.* **290**, 111223 (2019).
8. Gireesha, B. J., Mahanthesh, B., Thammanna, G. T. & Sampathkumar, P. B. Hall effects on dusty nanofluid two-phase transient flow past a stretching sheet using KVL model. *J. Mol. Liq.* **256**, 139–147 (2018).

9. Firdous, H., Husnine, S. M., Hussain, F. & Nazeer, M. Velocity and thermal slip effects on two-phase flow of MHD Jeffrey fluid with the suspension of tiny metallic particles. *Phys. Scr.* **96**(2), 025803 (2020).
10. Sohail, M., Shah, Z., Tassaddiq, A., Kumam, P. & Roy, P. Entropy generation in MHD Casson fluid flow with variable heat conductance and thermal conductivity over non-linear bi-directional stretching surface. *Sci. Rep.* **10**(1), 1–16 (2020).
11. Hamid, A. Numerical study of temperature dependent thermal conductivity and homogeneous–heterogeneous reactions on Williamson fluid flow. *J. Phys. Commun.* **4**(8), 085009 (2020).
12. Ramadevi, B., Kumar, K. A., Sugunamma, V. & Sandeep, N. Influence of non-uniform heat source/sink on the three-dimensional magnetohydrodynamic Carreau fluid flow past a stretching surface with modified Fourier's law. *Pramana* **93**(6), 1–11 (2019).
13. Lu, D. C., Ramzan, M., Bilal, M., Chung, J. D. & Farooq, U. Upshot of chemical species and nonlinear thermal radiation on Oldroyd-B nanofluid flow past a bi-directional stretched surface with heat generation/absorption in a porous media. *Commun. Theor. Phys.* **70**(1), 071 (2018).
14. Ramzan, M., Bilal, M., Kanwal, S. & Chung, J. D. Effects of variable thermal conductivity and non-linear thermal radiation past an Eyring Powell nanofluid flow with chemical Reaction. *Commun. Theor. Phys.* **67**(6), 723 (2017).
15. Gbadeyan, J. A., Titiloye, E. O. & Adeosun, A. T. Effect of variable thermal conductivity and viscosity on Casson nanofluid flow with convective heating and velocity slip. *Heliyon* **6**(1), e03076 (2020).
16. Irfan, M., Khan, M. & Khan, W. A. Interaction between chemical species and generalized Fourier's law on 3D flow of Carreau fluid with variable thermal conductivity and heat sink/source: A numerical approach. *Results Phys.* **10**, 107–117 (2018).
17. Lu, D. *et al.* MHD boundary layer flow of Carreau fluid over a convectively heated bidirectional sheet with non-Fourier heat flux and variable thermal conductivity. *Symmetry* **11**(5), 618 (2019).
18. Samrat, S. P., Reddy, M. G. & Sandeep, N. Buoyancy effect on magnetohydrodynamic radiative flow of Casson fluid with Brownian moment and thermophoresis. *Eur. Phys. J. Spec. Top.* **230**, 1–9 (2021).
19. Magagula, V. M., Shaw, S. & Kairi, R. R. Double dispersed bioconvective Casson nanofluid fluid flow over a nonlinear convective stretching sheet in suspension of gyrotactic microorganism. *Heat Transf.* **49**(5), 2449–2471 (2020).
20. Shaw, S., Mabood, F., Muhammad, T., Nayak, M. K., & Alghamdi, M. Numerical simulation for entropy optimized nonlinearradiative flow of GO-Al$_2$O$_3$ magneto nanomaterials with auto catalysis chemical reaction. *Numer. Methods Partial Differ.Equ.* https://doi.org/10.1002/num.22623 (2020).
21. Ramzan, M., Bilal, M., Chung, J. D., Lu, D. C. & Farooq, U. Impact of generalized Fourier's and Fick's laws on MHD 3D second grade nanofluid flow with variable thermal conductivity and convective heat and mass conditions. *Phys. Fluids* **29**(9), 093102 (2017).
22. Nawaz, M., Rafiq, S., Qureshi, I. H. & Saleem, S. Combined effects of partial slip and variable diffusion coefficient on mass and heat transfer subjected to chemical reaction. *Phys. Scr.* **95**(3), 035222 (2020).
23. Riasat, S., Ramzan, M., Su, Y. L., Malik, M. Y. & Chinram, R. Comparative analysis of Yamada-Ota and Xue models for hybrid nanofluid flow amid two concentric spinning disks with variable thermophysical characteristics. *Case Stud. Therm. Eng.* **26**, 101039 (2021).
24. Prasad, K. V., Vaidya, H., Vajravelu, K., Manjunatha, G., Rahimi-Gorji, M., & Basha, H. Heat transfer analysis of three-dimensional mixed convective flow of an oldroyd-B nanoliquid over a slippery stretching surface. In *Defect and Diffusion Forum*, vol. 401, 164–182. (Trans Tech Publications Ltd, 2020).
25. Ibrahim, W. & Zemedu, C. Numerical solution of micropolar nanofluids with Soret, Dufor effects and multiple slip conditions. *J. Phys. Commun.* **4**(1), 015016 (2020).
26. Iftikhar, N., Baleanu, D., Husnine, S. M. & Shabbir, K. Magnetohydrodynamic mixed convection flow of Jeffery fluid with thermophoresis, Soret and Dufour effects and convective condition. *AIP Adv.* **9**(3), 035251 (2019).
27. Prasannakumara, B. C., Reddy, M. G., Thammanna, G. T. & Gireesha, B. J. MHD Double-diffusive boundary-layer flow of a Maxwell nanofluid over a bidirectional stretching sheet with Soret and Dufour effects in the presence of radiation. *Nonlinear Eng.* **7**(3), 195–205 (2018).
28. Khan, M. I., Hayat, T., Afzal, S., Khan, M. I. & Alsaedi, A. Theoretical and numerical investigation of Carreau–Yasuda fluid flow subject to Soret and Dufour effects. *Comput. Methods Programs Biomed.* **186**, 105145 (2020).
29. Bhatti, M. M., Khalique, C. M., Bég, T. A., Bég, O. A. & Kadir, A. Numerical study of slip and radiative effects on magnetic Fe$_3$O$_4$-water-based nanofluid flow from a nonlinear stretching sheet in porous media with Soret and Dufour diffusion. *Mod. Phys. Lett. B* **34**(02), 2050026 (2020).
30. Ramzan, M., Yousaf, F., Farooq, M. & Chung, J. D. Mixed convective viscoelastic nanofluid flow past a porous media with Soret–DuFour effects. *Commun. Theor. Phys.* **66**(1), 133 (2016).
31. Ramzan, M., Inam, S. & Shehzad, S. A. Three dimensional boundary layer flow of a viscoelastic nanofluid with Soret and Dufour effects. *Alex. Eng. J.* **55**(1), 311–319 (2016).
32. Hamid, M., Usman, M. & Haq, R. U. Wavelet investigation of Soret and Dufour effects on stagnation point fluid flow in two dimensions with variable thermal conductivity and diffusivity. *Phys. Scr.* **94**(11), 115219 (2019).
33. Sulochana, C., Payad, S. S., & Sandeep, N. Non-uniform heat source or sink effect on the flow of 3D Casson fluid in the presence of Soret and thermal radiation. In *International Journal of Engineering Research in Africa*, vol. 20 112–129. (Trans Tech Publications Ltd., 2016).
34. Tlili, I., Samrat, S. P. & Sandeep, N. A computational frame work on magnetohydrodynamic dissipative flow over a stretched region with cross diffusion: Simultaneous solutions. *Alex. Eng. J.* **60**(3), 3143–3152 (2021).
35. Sulochana, C., Samrat, S. P. & Sandeep, N. Numerical investigation of magnetohydrodynamic (MHD) radiative flow over a rotating cone in the presence of Soret and chemical reaction. *Propuls. Power Res.* **7**(1), 91–101 (2018).
36. Shaw, S., Mahanta, G. & Das, M. Thermal and solutal Marangoni stagnation point Casson fluid flow over a stretching sheet in the presence of radiation, Soret and Dofour effect with chemical reaction. *Heat Transf. Asian Res.* **48**(1), 323–342 (2019).
37. Ullah, I., Khan, I. & Shafie, S. Soret and Dufour effects on unsteady mixed convection slip flow of Casson fluid over a nonlinearly stretching sheet with convective boundary condition. *Sci. Rep.* **7**(1), 1–19 (2017).
38. Ramzan, M., Bilal, M., & Chung, J. D. Soret and Dufour effects on three dimensional upper-convected Maxwell fluid with chemical reaction and non-linear radiative heat flux. *Int. J. Chem. React. Eng.* **15**(3), 2016–0136 (2017).
39. Jawad, M., Saeed, A. & Gul, T. Entropy generation for MHD Maxwell nanofluid flow past a porous and stretching surface with Dufour and Soret effects. *Braz. J. Phys.* **51**, 1–12 (2021).
40. Megahed, A. M., Ghoneim, N. I., Reddy, M. G., & El-Khatib, M. Magnetohydrodynamic fluid flow due to an unsteady stretching sheet with thermal radiation, porous medium, and variable heat flux. *Adv. Astron.* **2021**, 6686883. https://doi.org/10.1155/2021/6686883 (2021).
41. Irfan, M., Farooq, M. A., Mushtaq, A. & Shamsi, Z. H. Unsteady MHD bionanofluid flow in a porous medium with thermal radiation near a stretching/shrinking sheet. *Math. Problems Eng.* **2020**, 1–14 (2020).
42. Rosali, H., Badlilshah, M. N., Johari, M. A. M. & Bachok, N. Unsteady boundary layer stagnation point flow and heat transfer over a stretching sheet in a porous medium with slip effects. *CFD Lett.* **12**(10), 52–61 (2020).
43. Fatunmbi, E. O., Ogunseye, H. A. & Sibanda, P. Magnetohydrodynamic micropolar fluid flow in a porous medium with multiple slip conditions. *Int. Commun. Heat Mass Transf.* **115**, 104577 (2020).
44. Baitharu, A. P., Sahoo, S. & Dash, G. C. Heat and mass transfer effect on a radiative second grade MHD flow in a porous medium over a stretching sheet. *J. Nav. Archit. Mar. Eng.* **17**(1), 51–66 (2020).

45. Agrawal, P. *et al.* Lie similarity analysis of MHD flow past a stretching surface embedded in porous medium along with imposed heat source/sink and variable viscosity. *J. Market. Res.* **9**(5), 10045–10053 (2020).
46. Mabood, F. & Das, K. Outlining the impact of melting on MHD Casson fluid flow past a stretching sheet in a porous medium with radiation. *Heliyon* **5**(2), e01216 (2019).
47. Ahmad, K. & Ishak, A. Magnetohydrodynamic (MHD) Jeffrey fluid over a stretching vertical surface in a porous medium. *Propuls. Power Res.* **6**(4), 269–276 (2017).
48. Al-Hossainy, A. F., Mohamed, R. E. & Mohamed, S. Z. SQLM for external yield stress effect on 3D MHD nanofluid flow in a porous medium. *Phys. Scr.* **94**(10), 105208 (2019).
49. Kumar, B., Seth, G. S. & Nandkeolyar, R. Regression model and successive linearization approach to analyse stagnation point micropolar nanofluid flow over a stretching sheet in a porous medium with nonlinear thermal radiation. *Phys. Scr.* **94**(11), 115211 (2019).
50. Tlili, I., Ramzan, M., Kadry, S., Kim, H. W. & Nam, Y. Radiative mhd nanofluid flow over a moving thin needle with entropy generation in a porous medium with dust particles and hall current. *Entropy* **22**(3), 354 (2020).
51. Tlili, I., Samrat, S. P., Sandeep, N. & Nabwey, H. A. Effect of nanoparticle shape on unsteady liquid film flow of MHD Oldroyd-B ferrofluid. *Ain Shams Eng. J.* **12**(1), 935–941 (2021).
52. Shaw, S., Dogonchi, A. S., Nayak, M. K. & Makinde, O. D. Impact of entropy generation and nonlinear thermal radiation on Darcy–Forchheimer flow of MnFe$_2$O$_4$-Casson/water nanofluid due to a rotating disk: Application to brain dynamics. *Arab. J. Sci. Eng.* **45**, 1–20 (2020).
53. Mahanta, G. & Shaw, S. 3D Casson fluid flow past a porous linearly stretching sheet with convective boundary condition. *Alex. Eng. J.* **54**(3), 653–659 (2015).
54. Mishra, S. R., Khan, M. I. & Rout, B. C. Dynamics of dust particles in a conducting dusty nanomaterials: A computational approach. *Int. Commun. Heat Mass Transf.* **119**, 104967 (2020).
55. Nagaraja, B., Gireesha, B. J., Sowmya, G. & Krishnamurthy, M. R. Slip and radiative flow of shape dependent dusty nanofluid over a melting stretching sheet. *Int. J. Ambient Energy* **1**, 1–12 (2020).
56. Nabwey, H. A. & Mahdy, A. Transient flow of Micropolar dusty hybrid nanofluid loaded with Fe$_3$O$_4$–Ag nanoparticles through a porous stretching sheet. *Results Phys.* **21**, 103777 (2021).
57. Ramzan, M., Abid, N., Lu, D. & Tlili, I. Impact of melting heat transfer in the time-dependent squeezing nanofluid flow containing carbon nanotubes in a Darcy–Forchheimer porous media with Cattaneo–Christov heat flux. *Commun. Theor. Phys.* **72**(8), 085801 (2020).
58. Joshi, N., Upreti, H., Pandey, A. K. & Kumar, M. Heat and mass transfer assessment of magnetic hybrid nanofluid flow via bidirectional porous surface with volumetric heat generation. *Int. J. Appl. Comput. Math.* **7**(3), 1–17 (2021).
59. Ramzan, M., Gul, H., Kadry, S. & Chu, Y. M. Role of bioconvection in a three dimensional tangent hyperbolic partially ionized magnetized nanofluid flow with Cattaneo–Christov heat flux and activation energy. *Int. Commun. Heat Mass Transf.* **120**, 104994 (2021).
60. Reddy, M. V. & Lakshminarayana, P. Cross-diffusion and heat source effects on a three-dimensional MHD flow of Maxwell nanofluid over a stretching surface with chemical reaction. *Eur. Phys. J. Spec. Top.* **230**, 1–9 (2021).
61. Waqas, H., Imran, M. & Bhatti, M. Bioconvection aspects in non-Newtonian three-dimensional Carreau nanofluid flow with Cattaneo–Christov model and activation energy. *Eur. Phys. J. Spec. Top.* **230**, 1–14 (2021).
62. Mahanthesh, B. & Gireesha, B. J. Scrutinization of thermal radiation, viscous dissipation and Joule heating effects on Marangoni convective two-phase flow of Casson fluid with fluid-particle suspension. *Results Phys.* **8**, 869–878 (2018).
63. Mohaghegh, M. R., & Rahimi, A. B. Three-dimensional stagnation-point flow and heat transfer of a dusty fluid toward a stretching sheet. *J. Heat Transfer.* **138**(11), 112001 (2016).
64. Sajid, T., Sabir, Z., Tanveer, S., Arbi, A., & Altamirano, G. C. Upshot of radiative rotating Prandtl fluid flow over a slippery surface embedded with variable species diffusivity and multiple convective boundary conditions. *Heat Transf.* **50**(3), 2874–2894 (2020).
65. Sajid, T., Sagheer, M., & Hussain, S. Impact of temperature-dependent heat source/sink and variable species diffusivity on radiative Reiner–Philippoff fluid. *Math. Problems Eng.* **2020**, 9701860. https://doi.org/10.1155/2020/9701860 (2020).
66. Mallikarjuna, H. B., Jayaprakash, M. C. & Mishra, R. Three-dimensional boundary layer flow and heat transfer of a fluid particle suspension over a stretching sheet embedded in a porous medium. *Nonlinear Eng.* **8**(1), 734–743 (2019).
67. Gireesha, B. J., Shankaralingappa, B. M., Prasannakumar, B. C., & Nagaraja, B. MHD flow and melting heat transfer of dusty Casson fluid over a stretching sheet with Cattaneo–Christov heat flux model. Int. J. Ambient Energy, 785938. https://doi.org/10.1080/01430750.2020.1 (2020).
68. Wang, C. Y. The three-dimensional flow due to a stretching flat surface. *Phys. Fluids* **27**(8), 1915–1917 (1984).

Author contributions
M.R. supervised and conceived the idea; N.S wrote the manuscript and did the software work. A.A. and P.K. helped in revising the manuscript. Z.S. worked on the software and the funding arrangements.

Funding

Competing interests
The authors declare no competing interests.

Additional information
Correspondence and requests for materials should be addressed to Z.S. or P.K.

Reprints and permissions information is available at www.nature.com/reprints.

Publisher's note Springer Nature remains neutral with regard to jurisdictional claims in published maps and institutional affiliations.